Transportation Geotechnics 30 (2021) 100616

Contents lists available at ScienceDirect

Transportation Geotechnics

journal homepage: www.elsevier.com/locate/trgeo

Deformation characteristics of medium-dense sand-clay mixtures under a principal stress rotation

Halil Ibrahim Fedakar [a,*], Bora Cetin [b], Cassandra J. Rutherford [c]

[a] Department of Civil Engineering, Abdullah Gul University, 38080 Kayseri, Turkey
[b] Department of Civil and Environmental Engineering, Michigan State University, 48824 East Lansing, MI, USA
[c] Department of Civil, Construction and Environmental Engineering, Iowa State University, 50011 Ames, IA, USA

ARTICLE INFO

Keywords:
A principal stress rotation
A heart-shaped stress path
Hollow cylinder test
Triaxial test
Medium-dense sand-clay mixtures

ABSTRACT

A moving wheel load induces a principal stress rotation (PSR) in pavement foundation geomaterials including subgrade/subbase soils. Simulating such a stress condition is not possible with stress path tests conducted with conventional cyclic triaxial (CT) equipment. More complex stress paths such as a heart-shaped stress path are required to determine the deformation characteristics of these under a PSR. A heart-shaped stress path can be simulated on a soil specimen in cyclic hollow cylinder (CHC) tests via user-defined waveforms for its stress components (axial stress, and torsional shear stress). In this study, a series of CT and CHC tests were performed to analyze the impact of a PSR on strain behaviors of medium-dense sand-clay mixtures. The specimens contained 0%, 5%, 10%, and 20% clay by weight and were prepared at an initial relative density of 50%. All specimens were anisotropically consolidated under $K_0 \approx 0.5$. It was determined that all CT specimens underestimated the strain performances (both axial strain and shear strain) of the sand-clay mixtures. On the other hand, a heart-shaped stress path was simulated successfully in CHC tests and thus, all specimens yielded more accurate strain results. At low clay content ($\leq$10%), the impact of a PSR on strain performances of the sand-clay mixtures was observed to be less (axial strain (ε_z) $< 0.12\%$, and shear strain ($\gamma_{z\theta}$) $< 0.8\%$ after number of load cycles (N) = 5000) due to the low stress ratios ($CVSR = 0.15$ and $\eta = 1/3$). On the other hand, despite the low stress ratios, a PSR caused a rapid increase in axial strain and shear strain ($\varepsilon_z = 5\%$, and $\gamma_{z\theta} > 0.8\%$) of the specimen containing 20% clay, which resulted in the failure of the specimen at $N = 478$. Results of this study clearly indicated that the effect of a PSR should be taken into consideration while evaluating the strain characteristics of the sand-clay mixtures that contain clay particularly at high contents ($\geq$20%) under traffic loads.

Introduction

The permanent deformation of pavement foundation layers (i.e., base, subbase, and subgrade) is one of the main distresses in pavement systems. Pavement structures may be subjected to excessive deformations under traffic loads during their service life. This causes failures in pavement structures (i.e., rutting) and consequently requires major maintenance costs particularly in flexible pavements (Puppala et al., 1999, 2009; Chai and Miura, 2002; Korkiala and Dawson, 2007; Haider et al., 2014, Cetin et al., 2014; Li et al., 2019; Fedakar et al., 2020). This problem can be overcome by a better understanding of the deformation behavior of soils/geomaterials in pavement foundation layers. Therefore, there has been experimental studies in the literature that has investigated the deformation behavior of soils under long-term traffic loading through a series of laboratory tests in recent years (Alnedawi et al., 2018, 2019; Cai et al., 2015, 2017, 2018; Cetin et al., 2014; Cui, 2018; Frost et al., 2004; Georgiannou and Konstadinou, 2014; Guimaraes et al., 2019; Guo et al., 2016, 2018; Haider et al., 2014; Kim and Kim, 2007; Li et al., 2019; Noolu et al., 2019; Qian et al., 2016; Saberian and Li, 2019; Saberian et al., 2019; Shen et al., 2017; Yang et al., 2019). In these studies, conventional cyclic triaxial tests were commonly employed to impose the in-situ stress states on soil specimens. However, the studies using more advanced testing systems indicated that the change in the magnitude and direction of the principal stresses that act on a soil particle happens by a moving wheel load, resulting in a principal stress rotation (PSR) (Cai et al., 2015; Guo et al., 2016, 2018; Qian et al., 2016). Since the reliability and accuracy of test results highly depend on how well the actual field stress states are

* Corresponding author.
E-mail address: halilibrahim.fedakar@agu.edu.tr (H.I. Fedakar).

https://doi.org/10.1016/j.trgeo.2021.100616
Received 11 February 2021; Received in revised form 22 June 2021; Accepted 5 July 2021
Available online 9 July 2021

simulated in a laboratory test setup, the PSR induced by a moving wheel load needs to be considered in such experimental investigations. Two of three principal stresses (σ_1: major principal stress, σ_2: intermediate principal stress, and σ_3: minor principal stress) are kept equal ($\sigma_2 = \sigma_3$) during a conventional triaxial test, causing a major principal stress to be either parallel (PSR = 0°) or perpendicular (PSR = 90°) to the vertical direction (Guo et al., 2016). In addition, the triaxial specimens are only subjected to a vertical load (or stress). On the contrary, shear stress and vertical stress should be simultaneously applied on a specimen for a more accurate laboratory simulation of the PSR. Due to these limitations of triaxial tests, a conventional triaxial testing system is not capable of applying such a PSR on specimens. For the simulation of PSR, Cai et al. (2015), Guo et al. (2016), and Qian et al. (2016) reported that a heart-shaped stress path including both shear stress and vertical stress can be used to simulate the PSR in a laboratory test setup.

A hollow cylinder testing system enables researchers to independently control four degrees of load components (i.e., vertical stress (σ_z), radial stress (σ_r), circumferential stress (σ_θ), and shear stress ($\tau_{z\theta}$)). This system can therefore impose a PSR resulting from complex stress paths on a specimen (Cai et al., 2015; Guo et al., 2018; Qian et al., 2018). As mentioned earlier, a heart-shaped stress path involves both shear stress ($\tau_{z\theta}$) and vertical stress (σ_z) in a deviatoric stress space ($\tau_{z\theta}$ to (σ_z- σ_θ)/2). Due to the above features of the system, some researchers have successfully performed hollow cylinder tests on soil specimens for a better simulation of the PSR induced by a heart-shaped stress path in the last decade (Cai et al., 2015, 2017, 2018; Georgiannou and Konstadinou, 2014; Guo et al., 2016, 2018; Qian et al., 2016; Yang et al., 2019; Fedakar et al., 2020). Previous studies also examined the impact of a heart-shaped stress path on soils' deformation performances by triaxial tests as well as hollow cylinder tests (Guo et al., 2018; Cai et al., 2015, 2017, 2018; Fedakar et al., 2020; Qian et al., 2016). In these studies, a stress path that was along the horizontal axis ((σ_z-σ_θ)/2) was applied on the triaxial specimens as the stress conditions for triaxial tests. On the other hand, a heart-shaped stress path was applied on the specimens in hollow cylinder tests. It was observed from the test results that the hollow cylinder specimens produced higher deformations than the triaxial specimens. It was also reported by Cai et al. (2018), Guo et al. (2018), and Qian et al. (2016) that a heart-shaped stress path may have more influence on other soil behaviors such as excess pore-water pressure, resilient modulus, damping ratio, stiffness degradation, and plastic shakedown compared to the stress path of triaxial tests.

In the abovementioned studies, sand and clay specimens were mostly tested to study the effect of a PSR induced by a heart-shaped stress path on soil behavior. However, in a pavement structure, sand-clay mixtures having clay at low amounts are also used as subbase and subgrade materials. Therefore, the behavior of these sand-clay mixtures under a PSR induced by traffic loading needs to be studied experimentally. For this purpose, Fedakar et al. (2020) performed CT and CHC tests to investigate the effect of the PSR on the deformation behavior of a sand-clay mixture. In this study, dense sand-clay specimens with 20% clay and an initial relative density of 80% were used. From the test results, it was reported that the compressibility behavior of clay may become more apparent in a dense sand-clay mixture under a PSR, which may cause a quick development of permanent deformation. However, since relative density and fine (i.e., silt and clay) content are the key parameters influencing the behavior of sand-fine mixtures (Belkhatir et al., 2011; Salgado et al., 2000; Simpson and Evans, 2016), more studies considering these parameters are required to better understand the deformation behavior of sand-clay mixtures under a PSR and heart-shaped stress path.

According to the previous studies mentioned above, a PSR should be taken into consideration in pavement design since it may have a considerable impact on the deformation development in soils under traffic loading. However, there are limited studies that examined the deformation behavior of sand-clay mixtures through a heart-shaped stress path. To address this gap in the literature, the impact of a PSR induced by a heart-shaped stress path on the deformation behavior and stress–strain responses of medium-dense sand-clay mixtures containing clay at low rates was investigated in this study. To achieve this goal, a series of CT and CHC tests were performed on medium-dense sand-clay specimens that contained clay at 0%, 5%, 10%, and 20% by weight. In the CHC tests, the specimens were subjected to a heart-shaped stress path for the simulation of the PSR. Moreover, a stress path along the horizontal axis ((σ_z-σ_θ)/2) in the deviatoric stress space was imposed on the CT specimens. The results from both tests were compared to better understand the effect of the PSR on the deformation development in medium-dense sand-clay mixtures.

Materials and Testing Conditions

Testing materials

Ottawa 50/70 sand and pulverized kaolin clay were used in sand-clay mixtures in the present study. The materials were commercially supplied from EMD Millipore Sigma Corporation and Edgar Minerals, respectively. Index properties and grain size distribution of materials are presented in Table 1 and Fig. 1, respectively. As seen in Table 1, these materials are classified as poorly graded sand (SP) and high plasticity clay (CH), respectively, as per the Unified Soil Classification System.

Specimen Preparation and Testing Procedure

Simpson and Evans (2016) reported about sand-clay mixtures that there is a critical fine content at which a minimum void ratio is obtained without displacing sand grains. The contact area of sand particles reduces as clay content increases (i.e., > critical fine content) and the behavior of clay correspondingly becomes more dominant in the mixture at higher contents. That may result in higher permanent deformations in pavement structures. The upper limit for the clay content was therefore determined in accordance with this concept of "critical fine content". For this, the minimum void ratios of sand-clay mixtures including clay at 0%, 5%, 10%, 20%, and 30% by dry weight were first calculated. The results indicated that the sand-clay mixture containing 20% clay yielded the minimum void ratio (0.53), which is shown in Fig. 2. Therefore, the clay content was limited to 20% in this study.

In this study, a hollow cylinder test apparatus was employed for both triaxial and hollow cylinder tests. Accordingly, all specimens including the ones for triaxial testing were prepared and tested in a hollow cylindrical shape with 200 mm in height, 60 mm in internal diameter, and 100 mm in outer diameter. These selected dimensions provided a minimization in stress non-uniformities in the specimens. By these dimensions, the boundary conditions also had no impact on the center of the specimen (Cai et al., 2015; Hight et al., 1983; Vaid et al., 1990). For the sand-clay mixtures, the clay material was added to the sand material at the rates of 0%, 5%, 10%, and 20% by weight and thereafter, the mixtures were manually mixed until a uniform mixture was achieved. The prepared mixtures were poured into a mold in a hollow cylindrical shape in 5 layers through a funnel and spoon. Throughout the pouring,

Table 1
Index properties of sand and clay used in this study.

Properties	Sand	Clay
Coefficient of uniformity (C_u)	1.22	–
Coefficient of curvature (C_c)	0.97	–
Minimum void ratio (e_{min})	0.61	–
Maximum void ratio (e_{max})	0.78	–
Liquid limit (LL) (%)	–	62
Plastic limit (PL) (%)	–	41
Classification (USCS)	SP	CH
Specific gravity (G_s)	2.65	2.65

Note: USCS = Unified soils classification system; SP = poorly graded sand; CH = high plasticity clay.

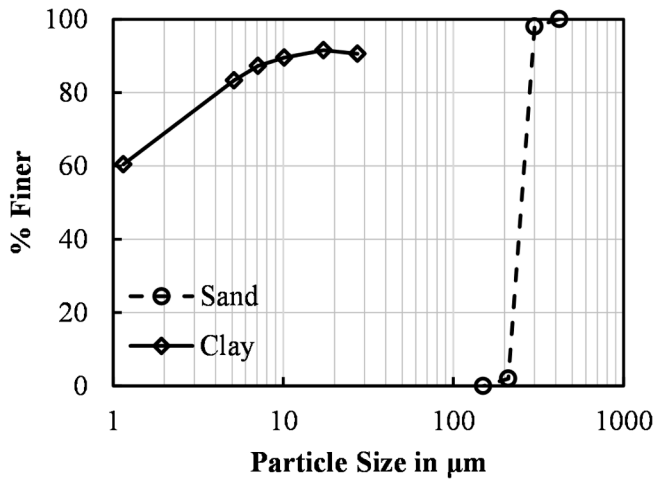

Fig. 1. Grain size distribution curves for Ottawa sand and kaolin clay used in this study.

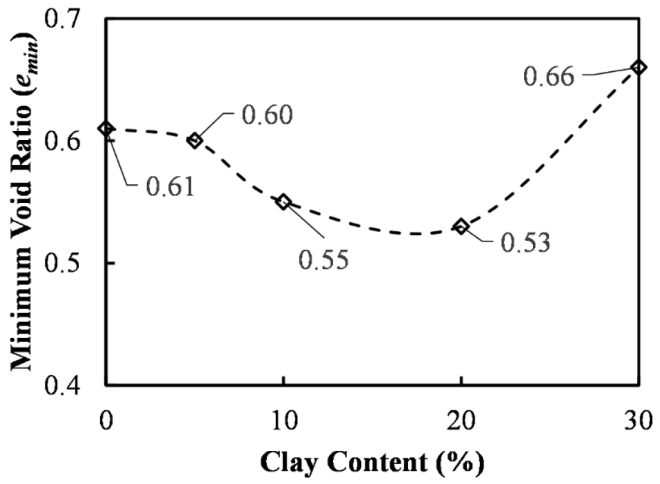

Fig. 2. The variation of minimum void ratio with clay contents.

the extreme care was taken and falling height was set to zero to prevent the segregation from occurring. Each layer was compacted to their target height (40 mm) by dry-tamping method so that the specimens had an initial relative density of 50%. Then, the specimens were placed in the hollow cylinder testing apparatus and the tubing connections for inner chamber, outer chamber, and back pressure were made. A vacuum pressure of 20 kPa was implemented to hold the specimens and to make the inner/outer membranes fully adhered to the walls of the mold. De-aired water was used to fill inner/outer chambers and controllers as well as back pressure controller. Inner and outer cell pressures of 30 kPa were applied to the specimens. The vacuum pressure was then released. Next, de-aired water was circulated from bottom to top of the specimen to remove the air from the specimens.

All triaxial and hollow cylinder tests in the current study had the following stages: (1) saturation, (2) K_0 consolidation (K_0: ratio of the effective horizontal stress to effective vertical stress), and (3) shearing. Stress non-uniformities take place along the specimen when inner cell pressure is not equal to outer cell pressure during testing. So, inner/outer cell pressures were kept equal throughout these three stages to minimize the stress non-uniformities (Mamou et al., 2018). All specimens were saturated under inner/outer cell pressures of 320 kPa and back pressure of 300 kPa (Cai et al., 2018). The inner/outer cell and back pressures were incrementally enhanced to their target values (320 kPa and 300 kPa, respectively). During this procedure, the effective confining pressure (=cell pressure-back pressure) of 20 kPa was kept constant. Skempton coefficient (B), the ratio of change in pore pressure to change in cell pressure, was used to determine if the specimens were saturated. The values of B>0.95 were obtained for all specimens by the end of the saturation, which indicated that all specimens were saturated. Thereafter, the specimens were consolidated with $K_0 \approx 0.5$ that is consistent with previous studies (Cai et al., 2017; Fedakar et al., 2020; Guo et al., 2018). At the consolidation stage, the vertical stress was initially increased to 340 kPa while the inner/outer cell pressures were kept constant (320 kPa). The vertical stress and inner/outer cell pressures were then simultaneously increased to 360 kPa and 330 kPa, respectively. In addition, the back pressure was kept constant (300 kPa) during this stress/pressure increment. By this way, $K_0 \approx 0.5$ was provided throughout the consolidation step of this study. It is well known that clay exhibits higher compressibility under loading than sand. Therefore, all specimens experienced different axial displacements after these two stages depending on the clay content used. For instance, 0% clay specimens had the lowest height change (1.5 ± 0.5 mm) while the specimen with 20% clay had the highest height change during the consolidation stage (Fig. 3a). Moreover, Fig. 3 shows that an increase in clay content yields an increase in height change during consolidation (as expected). The applied axial stress, inner/outer cell pressures, and back pressures during the saturation (Stage 1 to Stage 6) and consolidation (Stage 7 and Stage 8) shown in Fig. 3a were 50 kPa, 50 kPa, and 30 kPa in Stage 1, 100 kPa, 100 kPa, and 80 kPa in Stage 2, 150 kPa, 150 kPa, and 130 kPa in Stage 3, 200 kPa, 200 kPa, and 180 kPa in Stage 4, 250 kPa, 250 kPa, and 230 kPa in Stage 5, 320 kPa, 320 kPa, and 300 kPa in Stage 6, 340 kPa, 320 kPa, and 300 kPa in stage 7, and 360 kPa, 330 kPa, and 300 kPa in Stage 8, respectively. Fig. 3b shows the change in the height of the specimens (ΔH) over time in Stage 8. Consolidation results

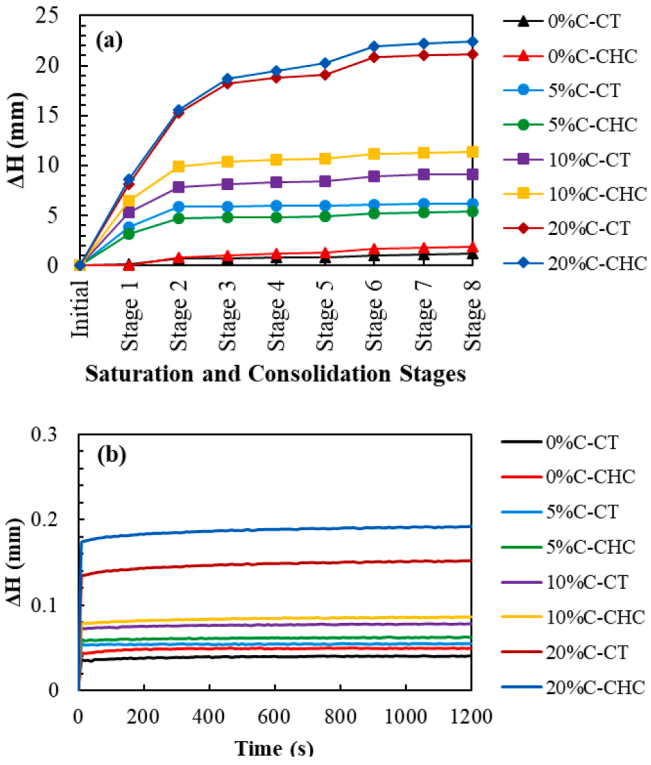

Fig. 3. The change in the height of the specimens (ΔH) (a) during saturation (Stage 1 to Stage 6) and consolidation (Stage 7 to Stage 8) and (b) over time during the consolidation (Stage 8) (0 %C-CT: CT specimen without clay; 0 %C-CHC: CHC specimen without clay; 5 %C-CT: CT specimen with 5% clay; 5 %C-CHC: CHC specimen with 5% clay; 10 %C-CT: CT specimen with 10% clay; 10 %C-CHC: CHC specimen with 10% clay; 20 %C-CT: CT specimen with 20% clay; 20 %C-CHC: CHC specimen with 20% clay).

showed that all specimens were consolidated within a short time (<200 s) due to the relatively low clay contents (0%, 5%, 10%, and 20%) (Fig. 3b). Then, the specimens were sheared according to the experimental plan in Table 2 at the shearing stage. During this stage, insignificant change in pore water pressure (i.e., excess pore water pressure) (i.e., < 2 kPa in the specimens containing clay at 0%, 5%, and 10%, and < 3.7 kPa in the specimens with 20% clay) was measured due to low clay content (≤20%) and low cyclic vertical stress ratio ($CVSR = 0.15$). As a result, the evolution of excess pore water pressure and its effect on the behavior of sand-clay specimens was negligible in this study. In Table 2, cyclic triaxial and hollow cylinder tests were denoted as CT and CHC, respectively. The test IDs of CT10 and CHC10 represent the cyclic triaxial and hollow cylinder tests on the specimens containing 10% clay. Furthermore, σ_z^{amp}, $\tau_{z\theta}^{amp}$, η, $CVSR$, f, and N in Table 2 are the amplitudes of cyclic vertical stress, amplitudes of cyclic torsional shear stress, cyclic torsional stress ratio (σ_z^{amp} / $\tau_{z\theta}^{amp}$), cyclic vertical stress ratio (σ_z^{amp} / $2p'_0$), frequency, and number of load cycles, respectively. The p'_0 in cyclic vertical stress ratio is the initial mean effective stress ($=\sigma'_{z0} + \sigma'_{r0} + \sigma'_{\theta0})/3$) ($\sigma'_{z0}$: initial effective axial stress, σ'_{r0}: initial effective radial stress, and $\sigma'_{\theta0}$: initial effective circumferential stress) ($p'_0 = 40kPa$ in this study) (Cai et al., 2015). As seen in Table 2, the triaxial specimens were only subjected to cyclic vertical stress (12 kPa) to mimic the stress path in triaxial tests. On the other hand, the hollow cylinder specimens were cyclically imposed to both axial stress (12 kPa) and torsional shear stress (4 kPa) to simulate a heart-shaped stress path (Cai et al., 2017; Guo et al., 2018). According to the results of previous studies using heart shaped stress path, most of permanent deformations take place within the first 5000 load cycles (Cai et al., 2015, 2017; Guo et al., 2016, 2018). Therefore, all specimens were subjected to 5000 load cycles. In addition, the loading frequency of 1 Hz was used in this study.

Testing Apparatus

A hollow cylinder apparatus (HCA) was used in all tests (i.e., triaxial and hollow cylinder) of this study. This testing system uses a hollow cylinder specimen that is 200 mm in height (H), 100 mm in outer diameter (d_o), and 60 mm in internal diameter (d_i). An HCA enables experimenters to independently control four degrees of load components. Therefore, complex stress paths and principal stress rotation can be simulated by an HCA (Cai et al. 2015; Guo et al. 2018; Qian et al., 2018; Wang et al. 2018). More detailed information on this apparatus can be found in Cai et al. (2015), Gräbe and Clayton (2009), Guo et al. (2018), Wang et al. (2018), and Xiong et al. (2015).

Stress-Strain Conditions

A hollow cylinder specimen is subjected to an axial load (W), torque (M_T), outer cell pressure (p_o), and inner cell pressure (p_i) by an HCA. The following stress and strain components can develop in a hollow cylinder specimen due to these loads: axial stress (σ_z), torsional shear stress ($\tau_{z\theta}$), radial stress (σ_r), circumferential stress (σ_θ), major principal stress (σ_1), intermediate principal stress (σ_2), minor principal stress (σ_3), axial strain (ε_z), shear strain ($\gamma_{z\theta}$), radial strain (ε_r), and circumferential strain (ε_θ). An illustration of the stress and strain states in a hollow cylinder specimen can be seen in Fig. 4. The θ and α in Fig. 4 also represent rotational displacement and rotational angle, respectively. Table 3 presents the equations by Hight et al. (1983) that were used for calculating the stress and strain components in the current study. The r_o, r_i, ΔH, u_o, u_i, θ, ε_1, ε_2, and ε_3 in Table 3 are outer radius, inner radius, axial displacement, outer radius movement of the wall of the specimen, inner radius movement of the wall of the specimen, rotational displacement, major principal strain, intermediate principal strain and minor principal strain, respectively.

Heart-Shaped Stress Path

A soil particle is subjected to a principal stress rotation (PSR) due to a moving wheel load, which is illustrated in Fig. 5. Such a PSR behavior can be simulated by a heart-shaped stress path in a laboratory test setup more accurately. A heart-shaped stress path involves axial stress (σ_z) and torsional shear stress ($\tau_{z\theta}$) in the deviatoric stress space ($\tau_{z\theta}$ to (σ_z-σ_θ)/2). Circumferential stress (σ_θ) and radial stress (σ_r) are also imposed to a specimen during this stress path by an HCA. The predefined waveforms in Fig. 6a were used for cyclic axial stress and cyclic torsional shear stress for simulating a heart-shaped stress path in Fig. 6b. The α in Fig. 6b is the angle of the major principal stress (σ_1) with respect to the vertical and varies between –π/2 and π/2 (Cai et al., 2015). These waveforms are mathematically defined in Eqs. (1) and (2).

$$\sigma_z^{cyc} = 0.5\sigma_z^{amp}\left[\frac{1}{2}cos\left(\frac{4\pi}{T}t\right) - cos\left(\frac{2\pi}{T}t\right) + \frac{1}{2}\right] \quad (1)$$

$$\tau_{z\theta}^{cyc} = 0.77\tau_{z\theta}^{amp}\left[sin\left(\frac{2\pi}{T}t\right) - \frac{1}{2}sin\left(\frac{4\pi}{T}t\right)\right] \quad (2)$$

where σ_z^{cyc}, $\tau_{z\theta}^{cyc}$, t and T are cyclic axial stress, cyclic torsional shear stress, elapsed time, and period (1 s in this study).

Results and Discussion

Stress Paths

As mentioned earlier, a CHC test can generate a heart-shaped stress path by applying axial stress (σ_z) and torsional shear stress ($\tau_{z\theta}$) simultaneously (Fig. 6). On the other hand, a CT test is capable of imposing only axial stress (σ_z) on a specimen, producing a stress path that is a straight line on the horizontal axis ((σ_z^{cyc}-σ_θ^{cyc})/2) of a deviatoric stress space ($\tau_{z\theta}^{cyc}$ to (σ_z^{cyc}-σ_θ^{cyc})/2). In this study, the CHC specimens were subjected to both axial stress and torsional shear stress simultaneously while only axial stress was applied on the CT specimens. Fig. 7 shows a typical

Table 2
The experimental plan followed in this study.

Test ID	Sand (%)	Clay (%)	Tests	σ_z^{amp} (kPa)	$\tau_{z\theta}^{amp}$ (kPa)	η	$CVSR$	f (Hz)	N
CT0	100	0	CT	12	0	0	0.15	1	5000
CT5	95	5							
CT10	90	10							
CT20	80	20							
CHC0	100	0	CHC	12	4	1/3	0.15	1	5000
CHC5	95	5							
CHC10	90	10							
CHC20	80	20							

Note: CT = cyclic triaxial test; CHC = cyclic hollow cylinder test; CT0 = the triaxial specimen containing 0% clay; CHC0 = the hollow cylinder specimen containing 0% clay; σ_z^{amp} = the amplitude of cyclic vertical stress; $\tau_{z\theta}^{amp}$ = the amplitude of cyclic torsional shear stress; η = cyclic torsional stress ratio; $CVSR$ = cyclic vertical stress ratio; f = frequency; N = number of load cycles.

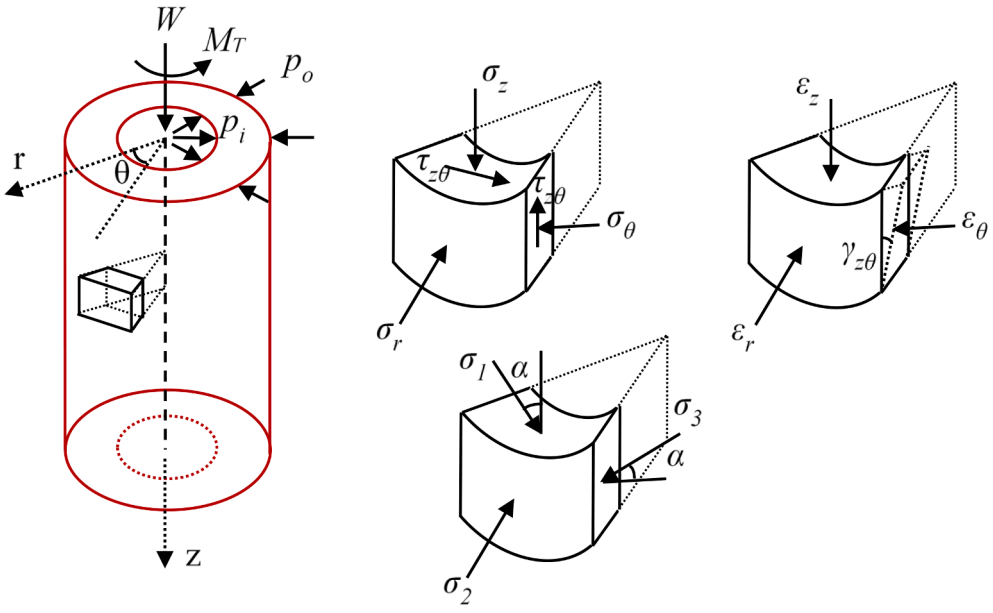

Fig. 4. Stress and strain states in a hollow cylinder specimen (Guo et al., 2018; Wang et al., 2018).

Table 3
The equations used for the stress and strain components (Hight et al., 1983).

Component	Stress	Strain
Axial	$\sigma_z = \frac{W}{\pi(r_0^2 - r_i^2)} + \frac{p_o r_0^2 - p_i r_i^2}{(r_0^2 - r_i^2)}$	$\varepsilon_z = \frac{\Delta H}{H}$
Circumferential	$\sigma_\theta = \frac{p_o r_o - p_i r_i}{(r_o - r_i)}$	$\varepsilon_\theta = \frac{u_o + u_i}{r_o + r_i}$
Radial	$\sigma_r = \frac{p_o r_o + p_i r_i}{(r_o + r_i)}$	$\varepsilon_r = \frac{u_o - u_i}{r_o - r_i}$
Shear	$\tau_{z\theta} = \frac{M_T}{2}\left[\frac{3}{2\pi(r_o^3 - r_i^3)} + \frac{4(r_o^3 - r_i^3)}{3\pi(r_o^2 - r_i^2)(r_o^4 - r_i^4)}\right]$	$\gamma_{z\theta} = \frac{\theta(r_o^3 - r_i^3)}{3H(r_o^2 - r_i^2)}$
Major principal	$\sigma_1 = \frac{\sigma_z + \sigma_\theta}{2} + \sqrt{\left(\frac{\sigma_z - \sigma_\theta}{2}\right)^2 + \tau_{z\theta}^2}$	$\varepsilon_1 = \frac{\varepsilon_z + \varepsilon_\theta}{2} + \sqrt{\left(\frac{\varepsilon_z - \varepsilon_\theta}{2}\right)^2 + \gamma_{z\theta}^2}$
Intermediate principal	$\sigma_2 = \sigma_r$	$\varepsilon_2 = \varepsilon_r$
Minor principal	$\sigma_3 = \frac{\sigma_z + \sigma_\theta}{2} - \sqrt{\left(\frac{\sigma_z - \sigma_\theta}{2}\right)^2 + \tau_{z\theta}^2}$	$\varepsilon_3 = \frac{\varepsilon_z + \varepsilon_\theta}{2} - \sqrt{\left(\frac{\varepsilon_z - \varepsilon_\theta}{2}\right)^2 + \gamma_{z\theta}^2}$

Note: σ_z = axial stress; σ_θ = circumferential stress; σ_r = radial stress; $\tau_{z\theta}$ = torsional shear stress; σ_1 = major principal stress; σ_2 = intermediate principal stress; σ_3 = minor principal stress; W = axial load; M_T = torque; p_o = outer cell pressure; p_i = inner cell pressure; r_o = outer radius; r_i = inner radius; ε_z = axial strain; ε_θ = circumferential strain; ε_r = radial strain; ε_1 = major principal strain; ε_2 = intermediate principal strain; ε_3 = minor principal strain; $\gamma_{z\theta}$ = shear strain; H = initial height of the specimen; ΔH = axial displacement; u_o = outer radius movement of the wall of the specimen; u_i = inner radius movement of the wall of the specimen; θ = rotational displacement.

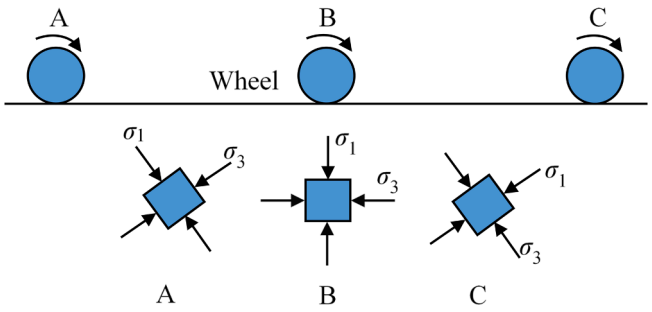

Fig. 5. The PSR acting on a soil particle while a moving wheel load (Guo et al., 2016).

example of target and applied stress waveforms (i.e., cyclic axial stress and torsional shear stress) and corresponding stress paths within a loading cycle. It is obvious in Fig. 7a that the axial stresses applied in both CT and CHC tests match well with the target axial stress. In addition, it can be said according to Fig. 7b that a satisfactory stress waveform for the torsional shear stress is achieved in CHC test. However, as expected, no torsional shear stress was measured in CT test (Fig. 7b). For the stress paths, the heart-shaped stress path and CT stress path applied in this study match well with their target stress paths as clearly observed in Fig. 7c. Based on the results from Fig. 7, it can be said that the test results presented here have an acceptable reliability for a better understanding of the deformation characteristics of medium-dense sand-clay mixtures under repeated traffic loads.

Effect of Principal Stress Rotation on Axial Strain Behavior

Axial Strain Development

Fig. 8 shows axial strain accumulations in CT and CHC specimens that contained 0%, 5%, 10%, and 20% clay with increasing number of load cycles. "*N*", "C", "CT", and "CHC" in Fig. 8 are the number of load cycles, clay, cyclic triaxial, and cyclic hollow cylinder specimens, respectively. In addition, "0%C-CT" and "0%C-CHC" in Fig. 8 represent cyclic triaxial and cyclic hollow cylinder specimens containing 0% clay, respectively. $\varepsilon_z \geq 5\%$ was adopted as a cyclic failure criterion of this study to determine whether a specimen fails (Vaid and Chern, 1983; Hyodo et al., 1991, 1994; Cheung, 1994; Li et al., 2011; Georgiannou and Konstadinou, 2014; Qian et al., 2016; Shen et al., 2017). Fig. 8

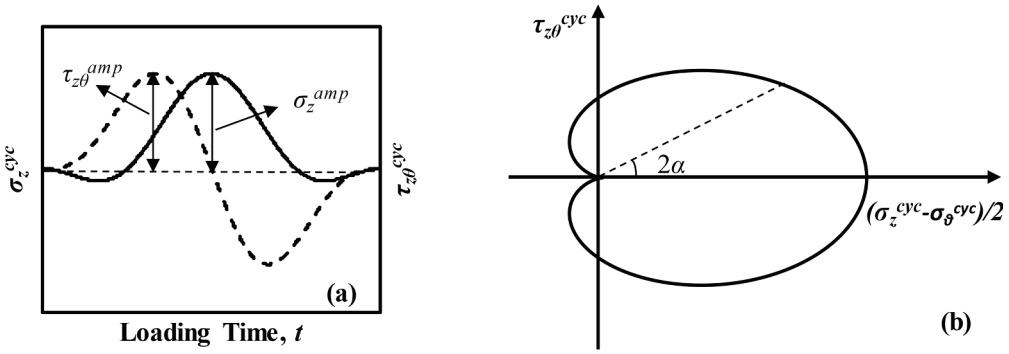

Fig. 6. Illustration of (a) the waveforms predefined for cyclic stresses and (b) a heart-shaped stress path.

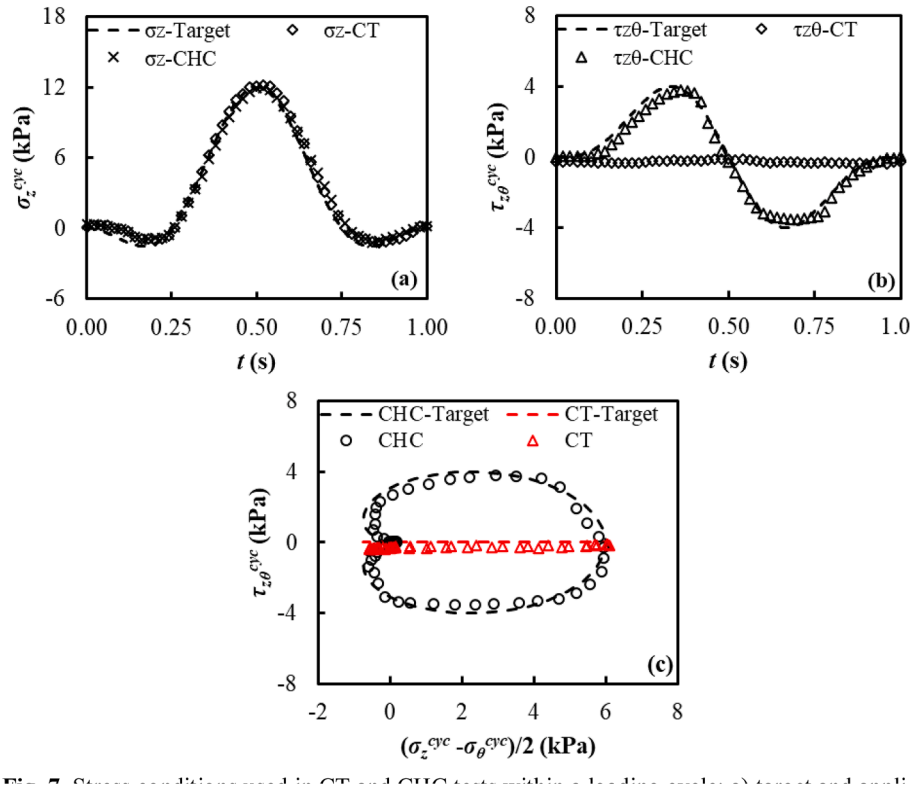

Fig. 7. Stress conditions used in CT and CHC tests within a loading cycle: a) target and applied waveforms for cyclic axial stress, b) target and applied waveforms for cyclic shear stress, and c) stress paths.

shows that most axial strain develops within the first 1000 load cycles in all specimens except for the specimen of 20 %C-CHC and then axial strain is growing steadily with increasing number of load cycles ($N \geq 1000$). Unlike the other specimens, a steady value for axial strain was not obtained in the specimen of 20 %C-CHC because it failed at $N = 478$ as a result of a sharp increase in axial strain. It is also clearly seen in Fig. 8 that the CHC specimens produced larger axial strain than the CT specimens. That could be attributed to the principal stress rotation induced by the heart-shaped stress path. On the other hand, Figs. 8a-8g indicate that the sand-clay specimens with 0%, 5%, 10%, and 20% clay exhibited axial strain<0.12% after 5000 load cycles, showing that they carried the applied loads without failure (i.e., $\varepsilon_z < 5\%$). It can be claimed from the test results (Figs. 8a-8f) that the principal stress rotation has a small impact on axial strain behavior of medium-dense sand-clay mixtures containing up to 10% clay (i.e., ≤10%). This could be due to low cyclic vertical stress ratio ($CVSR = 0.15$) used in this study since an axial strain behavior of soils under a principal stress rotation is highly dependent on stress ratios (Cai et al., 2015, 2018; Guo et al., 2018). In other words, the impact of a principal stress rotation may become more apparent as *CVSR* increases. In addition to stress ratios, clay content is another factor that influences axial strain behavior of a sand-clay mixture since clay can exhibit higher deformations than sand under same loading conditions. Regarding the clay content, Simpson and Evans (2016) reported that clay becomes more dominant in sand-clay mixtures at percentages greater than the critical fine content, resulting in the displacement of sand particles. Thus, it is expected that axial deformation under loading is mainly governed by sand particles in sand-clay mixtures with clay up to the critical fine content (≤20% for this study). Accordingly, the test results presented in Figs. 8a-8g could be also attributed to the critical fine content that was found to be 20% in this study at which a minimum void ratio (0.53) was obtained (Fig. 2). Nevertheless, a quick accumulation of axial strain developed in the 20 % C-CHC due to the principal stress rotation (Fig. 8h). As a result, the specimen 20 %C-CHC reached 5% axial strain at 478th load cycles and therefore, failed ($\varepsilon_z \geq 5\%$). This can be explained that the contact area between sand particles reduces significantly under the principal stress

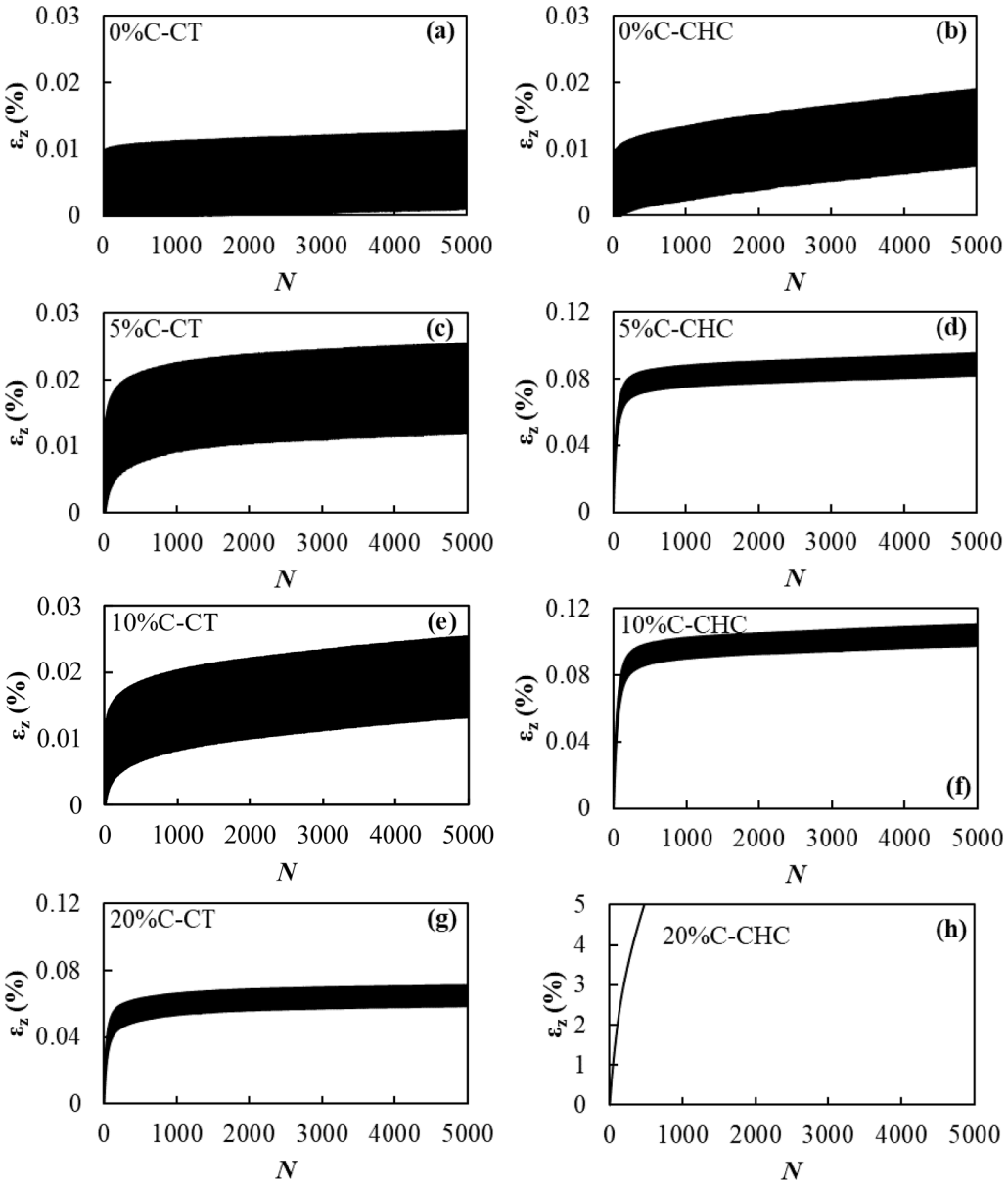

Fig. 8. Axial strain accumulation with the number of load cycles (*N*): a) CT specimen with 0% clay; b) CHC specimen with 0% clay; c) CT specimen with 5% clay; d) CHC specimen with 5% clay; e) CT specimen with 10% clay; f) CHC specimen with 10% clay; g) CT specimen with 20% clay; h) CHC specimen with 20% clay.

rotation despite low *CVSR* and critical fine content and consequently, clay particles govern the axial deformation development in a medium-dense sand-clay mixture with 20%. Based on these results, it can be claimed that the critical clay content for medium-dense sand-clay mixtures is 20% for CT tests. However, it is recommended that the sand-clay mixtures be studied for different clay contents (between 10% and 20%) via CHC tests further to ensure the critical clay content under a principal stress rotation. It can be concluded from the overall evaluation of the results in Figs. 8a-8h that the principal stress rotation may need to be taken into account for a better understanding of axial strain behavior of medium-dense sand-clay mixtures under repeated traffic loads, particularly as clay content (>20%) and stress ratios increase. Moreover, a quick growth of axial deformation due to PSR may lead failure in soils, as observed in the 20 %C-CHC (Fig. 8h). Thus, these results emphasize the importance of evaluating the impact of PSR on predicting soil behavior under traffic loads more accurately.

The concept of "shakedown" is employed to define permanent deformation behavior of soils under repeated traffic loads. Fig. 8 also provides results for the shakedown behavior of the sand-clay mixtures. Fig. 8 shows that all specimens (except the 20 %C-CHC) experience plastic creep behavior (a type of shakedown). In other words, increase rate of permanent axial strain decreases or remains nearly constant at a relatively low level after a large number of load cycles. It is also observed from the results in Fig. 8 that decrease in the permanent strain rate becomes smaller in the CHC specimens compared to the CT specimens. This indicates that the principal stress rotation influences shakedown behavior of sand-clay mixtures. However, this effect is determined to be insignificant for these specimens due to small axial stress applied and low clay content used in the sand-clay mixtures (i.e., ≤10%). Unlike the 20 %C-CT, the 20 %C-CHC exhibits ratchetting behavior (i.e., another type of shakedown) that result in an unstable increment in permanent axial strain with number of load cycles and failure of it in earlier cycles due to the excessive permanent axial strain (≥5%).

Figs. 8g-8h show that the principal stress rotation plays an important role on shakedown behavior of sand-clay mixtures with increasing clay content (≥20%) even under small axial stress. In addition, ratchetting behavior should always be avoided in field applications (Qian et al., 2016). For this reason, the principal stress rotation may need to be taken

into account for a more realistic evaluation of shakedown behavior of sand-clay mixtures under long-term traffic loads depending on clay content and the magnitude of axial stress applied.

Axial Stress-Strain Behavior

Axial stress–strain curves provide valuable insight about material behavior of soils and thus are important for a more accurate prediction of the deformation characteristics of soils. Moreover, the axial stress–-strain behavior of sand-clay mixtures may become time-dependent particularly with clay inclusion since clay soils exhibit time-dependent compression behavior under loads (Yin and Wang, 2012; Yin et al., 2015; Zhu et al., 2016). The axial stress–strain behaviors of the sand-clay mixtures under two different stress paths (i.e., the heart-shaped stress path, and CT stress path) are illustrated in Fig. 9. It is observed in Figs. 9a-9b that the CT and CHC specimens without clay (i.e., 0 %C-CT, and 0 %C-CHC) generate an elasto-plastic behavior with perfect plasticity. In other words, although the rearrangement of sand particles under the PSR causes larger axial strain in the 0 %C-CHC, the time-dependent (slow) axial strain develops in both specimens under a constant cyclic axial stress (12 kPa in this study). Similar behavior (an elasto-plastic behavior with perfect plasticity) is also observed for the 5 %C-CT and 10 %C-CT specimens (Figs. 9c and 9e). However, larger axial strain develops in these specimens under a constant cyclic axial stress due to the time-dependent compression behavior of clay. Moreover, the impact of clay content on the time-dependent axial stress–strain behavior of sand clay mixtures (containing clay $\leq$ 10%) is determined to be insignificant under the CT stress path, which could be explained by low stress ratio ($CVSR = 0.15$). On the other hand, the 5 %C-CHC and 10 %C-CHC exhibit strain hardening behavior where the applied axial stress tends to slightly rise with increasing axial strain (Figs. 9d and 9f), indicating that the PSR influences the time-dependent axial stress–strain behavior of sand-clay mixtures containing clay up to 10% (i.e., $\leq$10%). The 20 %C-CT specimen also exhibits strain hardening behavior (Fig. 9g), which implies that the effect of time-dependent behavior of clay on the stress–strain behavior of the CT specimens becomes apparent at high clay content (20% in this study). Conversely, 20 %C-CHC

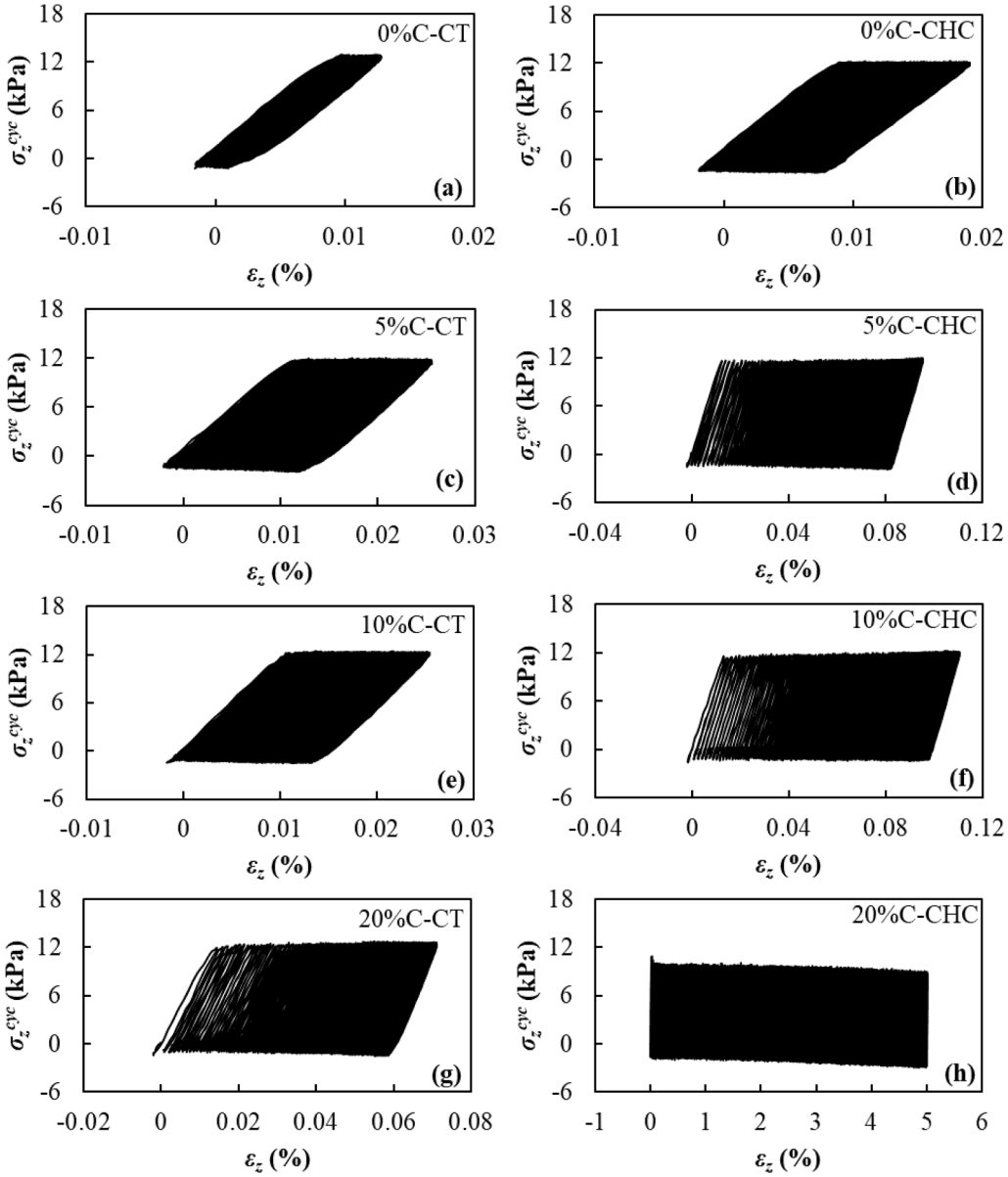

Fig. 9. Axial stress–strain behaviors of sand-clay mixtures under the CT stress path and heart-shaped stress path: a) CT specimen with 0% clay; b) CHC specimen with 0% clay; c) CT specimen with 5% clay; d) CHC specimen with 5% clay; e) CT specimen with 10% clay; f) CHC specimen with 10% clay; g) CT specimen with 20% clay; h) CHC specimen with 20% clay.

(Fig. 9h) performs strain softening behavior in which the axial stress gradually decreases (i.e., stress releases) with increasing axial strain. As a result of this, the 20 %C-CHC specimen weakens under the heart-shaped stress path, inducing an acceleration in permanent axial strain. Thus, it fails during earlier loading cycles ($N_{failure}$ = 478). It can be speculated that the PSR influences the material behavior of medium-dense sand-clay mixtures more than the presence of clay at low clay contents (<20%) (from an elasto-plastic behavior to strain hardening behavior). At a higher clay content (20% in this study), the material behavior also changes from strain hardening to strain softening due to the PSR even though small cyclic axial stress is applied. The effect of loading frequency on the axial stress–strain behavior of medium-dense sand-clay mixtures can be important too; however, it was not studied in this article.

Soil is not an elastic material and thus produces axial stress–strain hysteretic loops under cyclic loads (Guo et al., 2016). Fig. 10 shows the axial stress–strain hysteretic loops marked at different load cycles (N = 1, 100, 1000, 2000, 3000, 4000, and 5000 except for the specimen of 20 %C-CHC). For the CHC specimen with 20% clay, the hysteretic loops were plotted at N = 1, 100, and 478 since it failed at N = 478 ($\varepsilon_z \geq 5\%$) (Fig. 8h). Fig. 10 shows that the axial stress–strain loops of all CT and CHC specimens shift to the right implying that they are subjected to an increasing axial strain. According to the results shown in Figs. 10a-10b, almost half of the axial strain observed in the specimens without clay (i.e., 0 %C-CT, and 0 %C-CHC) takes place within the first 1000 load cycles. Then, the distance between loops reduces as the specimen approaches to a stable position in which the increase in axial strain tends to decrease. That results in denser axial stress–strain curves when the hysteretic loops coincide with the previous ones due to small axial strains. This is more apparent in the 0 %C-CT than the 0 %C-CHC since it produces smaller axial strains. Nevertheless, it can be claimed that both specimens give dense axial stress–strain curves over the entire load cycles (Figs. 9a-9b). Similar finding was also obtained from the 5 %C-CT and 10 %C-CT regarding the dense axial stress–strain curves (Figs. 9c and 9e). However, these specimens underwent approximately 80% of their axial strain within the first 1000 load cycles (Figs. 10c and 10e),

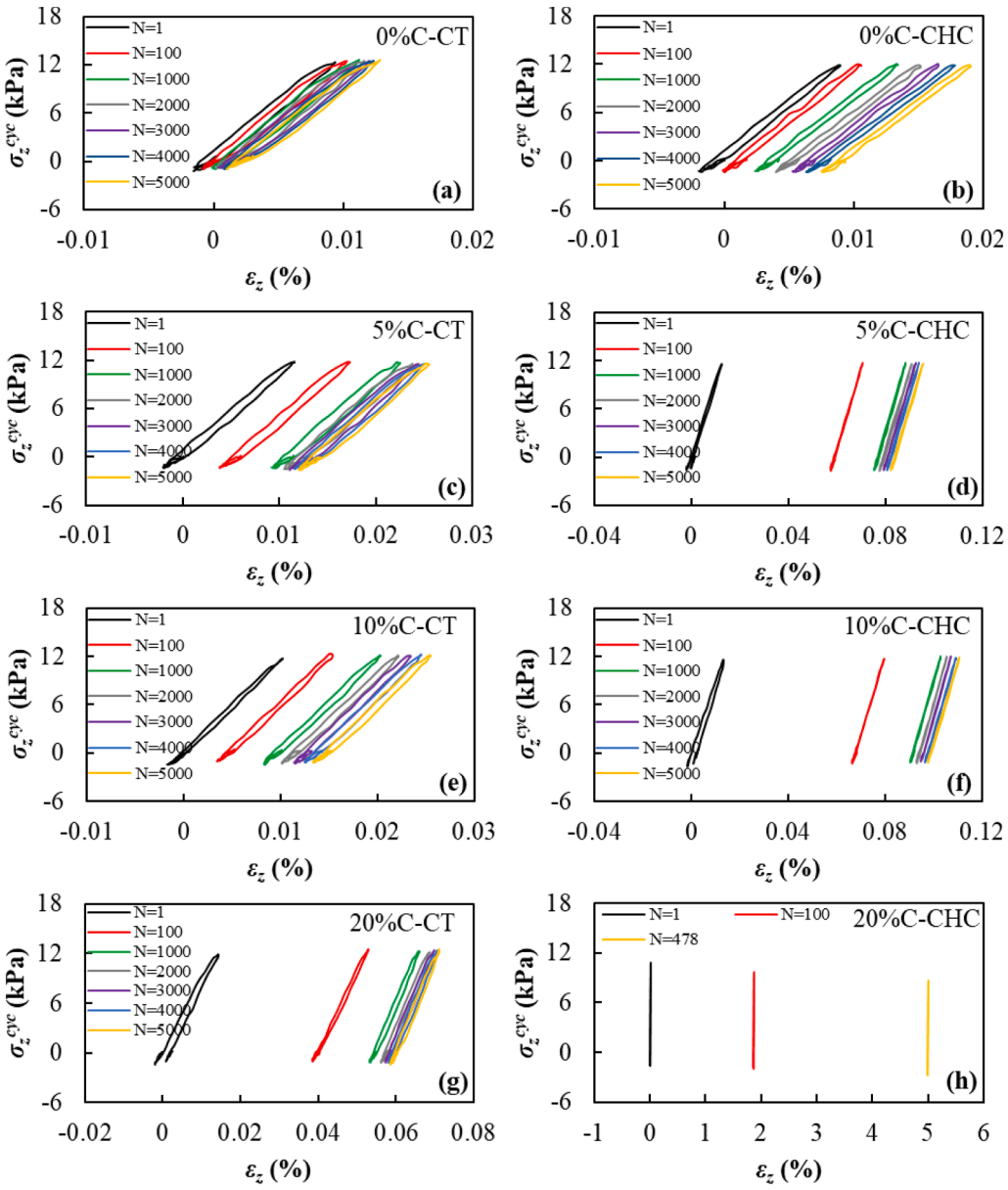

Fig. 10. Axial stress–strain hysteretic loops at different load cycles: a) CT specimen with 0% clay; b) CHC specimen with 0% clay; c) CT specimen with 5% clay; d) CHC specimen with 5% clay; e) CT specimen with 10% clay; f) CHC specimen with 10% clay; g) CT specimen with 20% clay; h) CHC specimen with 20% clay.

which is likely due to the presence of clay compared to the specimens without clay. On the other hand, as expected, the 5 %C-CHC, 10 %C-CHC, and 20 %C-CT produce initially sparse and then dense axial stress–strain curves (Figs. 9d, 9f, and 9g). The initial sparse curves obtained from these specimens indicate a relatively rapid increase in axial strain accumulation causing that>90% of the axial strain of these specimens developed within the first 1000 load cycles (Figs. 9d, 9f, and 9g). After 1000 load cycles, the loops nearly overlapped with the previous ones. Figs. 9e-9f show that the principal stress rotation may initially cause sparse curves even under small axial stress as a result of clay inclusion (i.e., higher axial strain development in earlier load cycles due to clay inclusion). 20 %C-CHC exhibited unstable behavior in terms of axial strain development due to the principal stress rotation. However, more sparse loops induced by a sharp increase in axial strain are not clearly seen in Fig. 9h due to the scale used for the horizontal axis.

Fig. 11 shows the axial stress–strain hysteretic loops that are translated to the original point to better analyze the dissipated energy characteristics of the sand-clay mixtures subjected to the CT and heart-shaped stress paths. Based on the results in Fig. 8, it can be said that most of the axial strain develops within the first 1000 load cycles and then the specimens perform nearly stabilized axial strain behavior. Therefore, the hysteretic loops in Figs. 11a-11g were plotted at $N = 1$, 100, 1000, and 5000 for the specimens that did not fail. As for the specimen that failed (i.e., 20 %C-CHC), the hysteretic loops were plotted at $N = 1$, 100, and 478, which is indicated in Fig. 11h. Dissipated energy (i.e., area of the hysteretic loops) influences microstructure of materials, which causes irrecoverable strain development and deterioration under cyclic loads (Tao et al., 2010; Yin and Chang, 2013; Qian et al., 2016). In other words, more energy dissipates as permanent strain increases which also results in opening of the hysteretic loops. On the other hand, the hysteretic loops can be nearly closed under very small permanent strain. The opening of the loops becomes more apparent in the specimen of 20

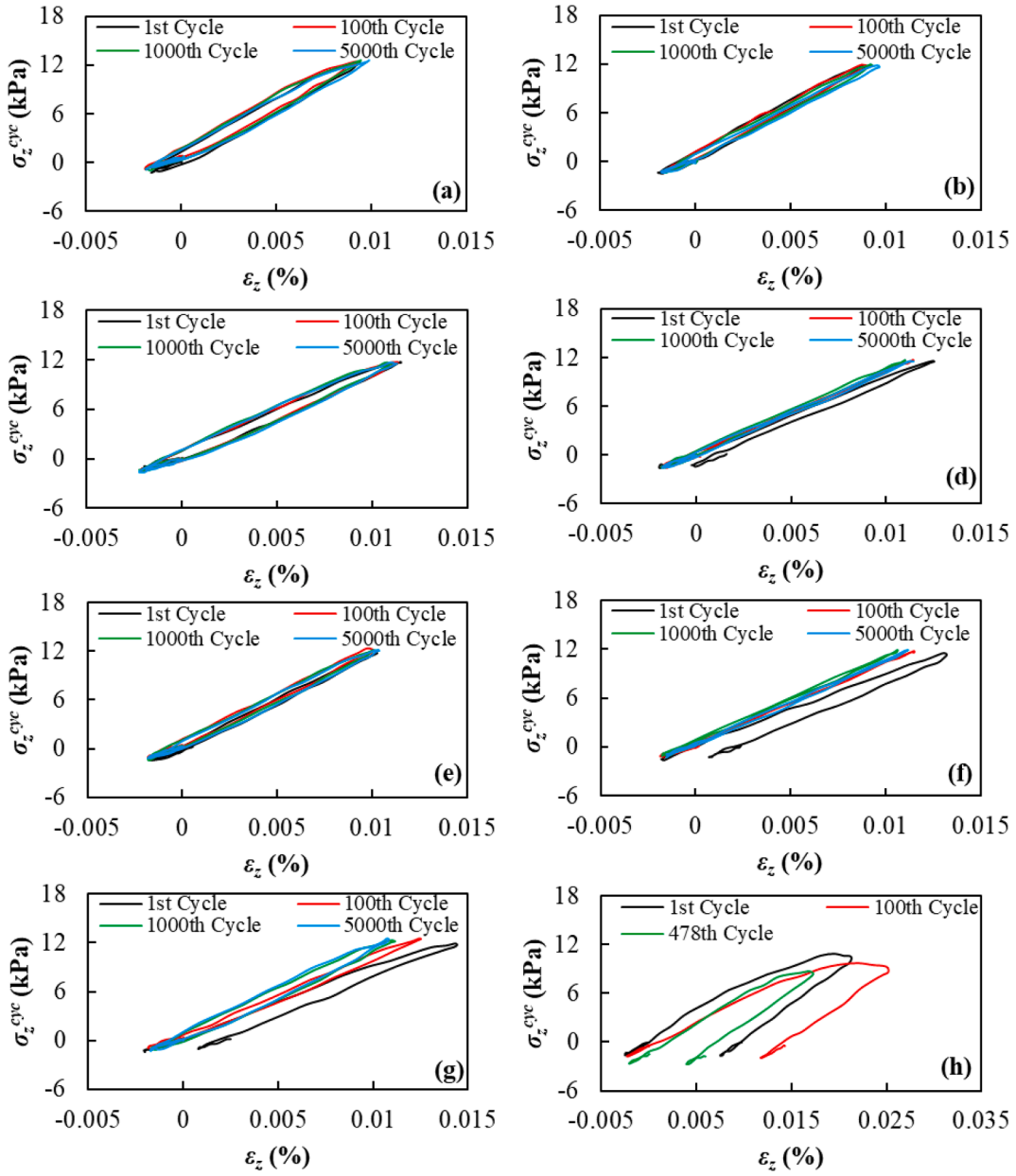

Fig. 11. The axial stress–strain loops at certain load cycles starting at the original point: a) CT specimen with 0% clay; b) CHC specimen with 0% clay; c) CT specimen with 5% clay; d) CHC specimen with 5% clay; e) CT specimen with 10% clay; f) CHC specimen with 10% clay; g) CT specimen with 20% clay; h) CHC specimen with 20% clay.

%C-CHC as a result of a quick accumulation of the permanent axial strain over the entire number of cycles ($N = 478$) (Fig. 11h). Furthermore, larger energy dissipation (i.e., larger area of the loops) is observed in 20 %C-CHC, causing the increase of irrecoverable strain (permanent strain). The opening of the hysteretic loops also occurs in the following specimens: 5 %C-CHC, 10 %C-CHC, and 20 %C-CT at $N = 1$ (Figs. 11d and 11f-11g). This is observed for these specimens since they produced the axial stress–strain hysteretic loops that are initially sparse resulting from a rapid increase of permanent strain in earlier cycles (Figs. 10d and 10f-10g). However, the loops are nearly closed in these specimens with increasing number of load cycles indicating very small development of permanent strain. The closed loops are also achieved in the specimens of 0 %C-CT, 0 %C-CHC, 5 %C-CT, and 10 %C-CT that performed very small permanent strain (Figs. 11a-11c and 11e). Based on the results from Fig. 11, it can be speculated that the area of the hysteretic loops is influenced by the principal stress rotation and clay content.

Effect of Principal Stress Rotation on Shear Strain

Shear Strain Development

Fig. 12 shows shear strain development in the CT and CHC specimens with number of load cycles (N). A logarithmic scale was used for the horizontal axes (i.e., N) in Fig. 12 to better indicate shear straining particularly during earlier cycles. In addition, while the shear strain vs number of load cycles curves in Figs. 12a-12g were plotted over the entire loading cycles ($N = 5000$), the curves in Fig. 12h were plotted until 478th load cycle at which the 20 %C-CHC failed ($\varepsilon_z \geq 5\%$). It is obvious in Fig. 12 that no shear strain developed in all CT specimens, which is because no torsional shear stress was applied in the CT tests of this study (i.e., $\eta = 0$). On the other hand, as shown in Fig. 12, the

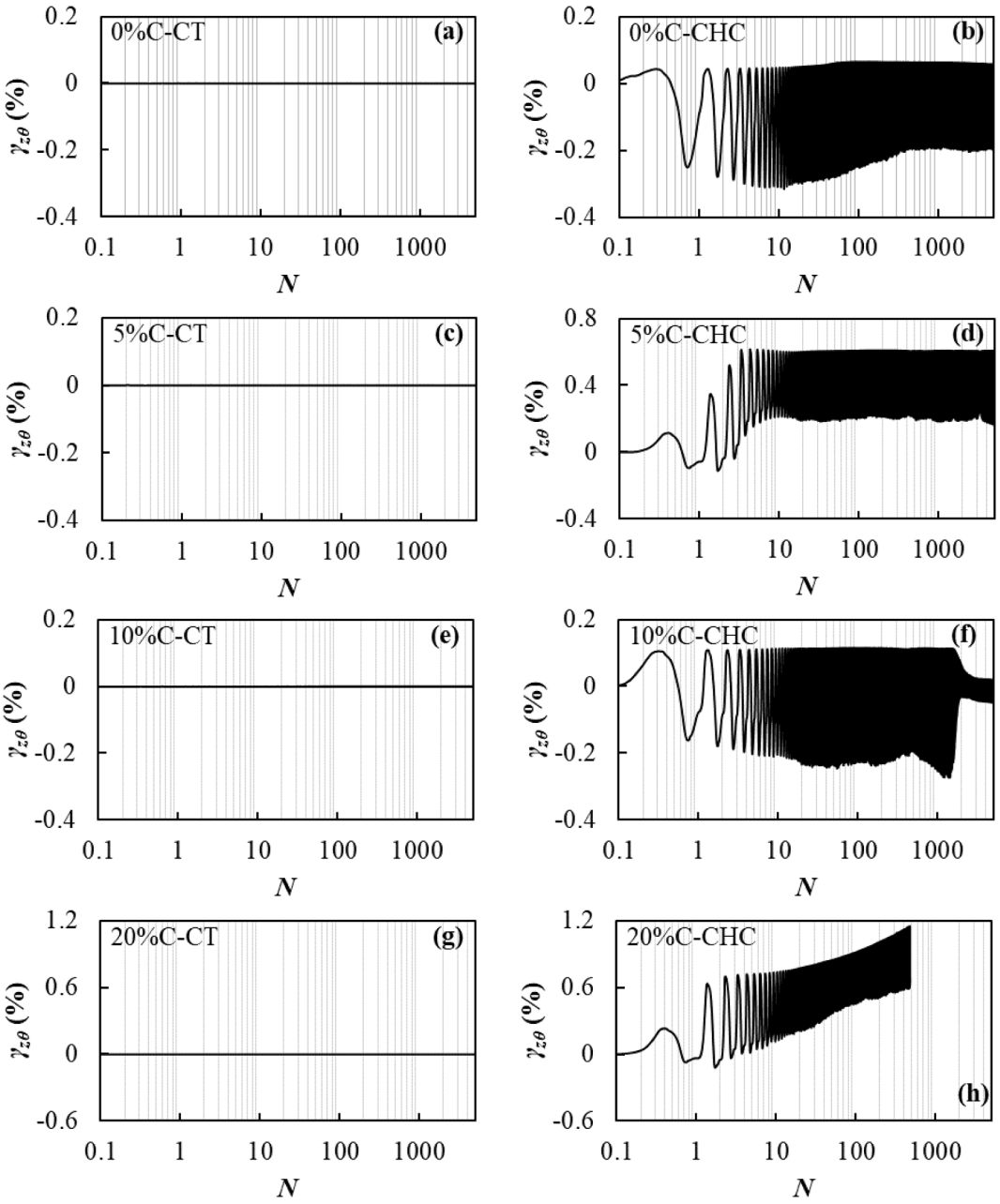

Fig. 12. Shear strain accumulation in CT and CHC specimens with the number of load cycles (N): a) CT specimen with 0% clay; b) CHC specimen with 0% clay; c) CT specimen with 5% clay; d) CHC specimen with 5% clay; e) CT specimen with 10% clay; f) CHC specimen with 10% clay; g) CT specimen with 20% clay; h) CHC specimen with 20% clay.

torsional shear stress ($\tau_{z\theta}^{amp} = 4$ kPa) induced shear strain development in all CHC specimens. In a loading cycle, the torsional shear stress was implemented as + 4 kPa in counterclockwise (i.e., compression or loading) direction at first and then –4 kPa in clockwise (i.e., extension or unloading) direction. While 4 kPa resulted in shear strain in compression (loading), −4 kPa produced shear strain in extension direction (unloading).

Figs. 12b, 12d, and 12f clearly show that the CHC specimens without failure yield shear strain performances<0.8% over the entire loading cycles ($N = 5000$). Moreover, they reached to a stable position in both directions after a finite number of load cycles, which means that no significant change occurred in shear strain with increasing load cycles. The CHC specimen with 0% clay exhibited negligible shear strain performances ($\gamma_{z\theta} < 0.1\%$) in compression (loading or counterclockwise direction) that were nearly constant over the entire loading cycles (Fig. 12b). This can be explained that the interlocking of sand particles quickly happened in this direction, causing no more rotation (shear strain). On the other hand, larger shear strains developed in extension (unloading or clockwise direction) throughout the test. This can be explained that strain softening behavior happened in this direction at $N = 10$. The strain softening behavior could be resulted from relaxation of the torsional shear stress (from + 4 kPa to – 4 kPa) in reverse (extension) direction. However, this specimen exhibited strain hardening behavior with increasing load cycles after $N = 10$ and reached to a stable level at approximately $N = 400$ in extension direction due to the interlocking of sand particles. As for the 5 %C-CHC, the shear strain accumulated cumulatively in compression until $N = 4$ (Fig. 12d). Then, it reached to a stable level for shear strain (i.e., no more shear strain) due to the interlocking of sand and clay particles. On the other hand, this specimen generated less shear strain in extension, indicating that the interlocking took place more quickly in this direction. According to the results in Figs. 12b and 12d, the 5 %C-CHC yielded larger shear strains, which was attributed to the clay addition since it has a higher compressibility characteristic than sand. Despite increasing clay content, less shear strain was accumulated in the 10 %C-CHC specimen compared to that of observed for the 5 %C-CHC specimen (Figs. 12d and 12f). In compression direction, the 10 %C-CHC specimen produced constant shear strain until approximately 2000 load cycles (Fig. 12f). After $N = 2000$, the shear strain decreased to a stable value due to the interlocking of sand and clay particles. Furthermore, most of the shear strain of the 10 %C-CHC developed in extension direction because of the strain softening behavior. The strain softening behavior continued until approximately $N = 2000$ at which the specimen started to exhibit strain hardening behavior and reached to a stable position quickly. Unlike the other specimens, the shear strain accumulated continuously in the 20 %C-CHC throughout the test (Fig. 12h). This can be explained that the 20% clay inclusion by weight significantly reduced the contact area between sand particles and thus less interlocking of sand particles happened under the principal stress rotation. In addition, it is observed that most of the shear strain developed for 20 %C-CHC in compression direction.

It is known that strain behavior of soils under a heart-shaped stress path is highly influenced by stress ratios (*CVSR* and η) as well as soil types (Cai et al., 2015, 2018; Guo et al., 2018). Large shear strain may develop in soft soils at low stress ratios, while higher stress ratios are required for large strain in granular soils. However, the impact of different *CVSR* and η values on strain behavior of the sand-clay mixtures was not within the scope of this study; therefore, it was not studied. Nevertheless, it can be claimed from the results of Fig. 12 together with the available literature that the effect of the principal stress rotation on shear strain development in the sand-clay mixtures may become more apparent irrespective of clay content with increasing stress ratios. Therefore, it needs to be taken into account while evaluating shear strain accumulation in sand-clay mixtures due to the principal stress rotation induced by a heart-shaped stress path.

Torsional Shear Stress-Strain Behavior

Fig. 13 illustrates the shear stress–strain performances of all CHC specimens for different clay contents (0%, 5%, 10%, and 20% by weight). To better understand the shear stress–strain behaviors of the CHC specimens with increasing number of load cycles, they were also plotted at different cyclic loads ($N = 1$, 10, 100, 1000, and 5000 except for the 20 %C-CHC) (Figs. 14a–14c). For the 20 %C-CHC, the shear stress–strain curves were plotted at $N = 1$, 10, 100 and 478 (Fig. 14d). Since no shear strain developed in the CT specimens (Fig. 12), the shear stress–strain curves of these specimens are not presented in Figs. 13-14. Fig. 13 clearly shows that the shear stress–strain curves are asymmetric indicating that all specimens exhibited different shear strain performances in loading (compression) and unloading (extension) directions in a loading cycle. The 0 %C-CHC and 10 %C-CHC generated most of the shear strain developed in unloading (extension) direction (Figs. 13a-13b). This can be explained that a better interlocking of soil particles was likely to occur in loading direction for these specimens. On the other hand, most of the shear strain of the 5 %C-CHC and 20 %C-CHC accumulated in loading direction. In addition, these specimens produced sparse shear stress–strain curves implying that the shear strain developed quickly.

As clearly seen in Fig. 14a, the 0 %C-CHC produced nearly linear hysteretic shear stress–strain loops and very small shear strains in compression, resulting in a small dissipated energy. This also confirms the findings presented in Fig. 12b where the 0 %C-CHC yields a very small shear strain and thus quickly reaches to a stable value for the shear strain in compression. On the other hand, according to Fig. 14a, the hysteretic loops firstly shift to the left in extension with increasing number of cycles indicating larger dissipated energy because of the strain softening behavior in this direction. Then, the loops move to the right after a small number of load cycles ($N > 10$), which is likely to occur due to the hardening behavior. It is obvious in Fig. 14a that the loops coincide with the previous ones with increasing number of load cycles implying that a stable shear strain position for the specimen is reached in both directions.

Fig. 14b shows that there is the large distance between the hysteretic loops during the earlier cycles of the test and then the loops nearly coincide with the previous ones as the number of load cycles rises. The large distances between the loops were likely to occur due to the clay addition as well as the principal stress rotation. This finding agrees with the results in Fig. 12d where the specimen performs a shear strain that firstly accumulated rapidly in compression due to the strain softening and then stabilizes in both directions after a small number of load cycles ($N > 4$). Furthermore, most of the energy dissipated in compression direction, which resulted in a higher shear strain development. Even though the higher shear strain developed in earlier cycles, less dissipated energy was observed at $N = 1$ (Fig. 14b). The less dissipated energy is the result of lower torsional shear stress. The high shear strain of this specimen accounts for the lower torsional shear stress obtained in earlier cycles (Fig. 14b). It is also seen that the torsional shear stress applied reached to its target value (4 kPa) after a small number of load cycles.

Fig. 14c clearly shows that the shear stress–strain hysteretic loops extend to the left meaning that the strain softening takes place in the extension direction of the 10 %C-CHC. As a result of the strain softening, this specimen generated higher shear strain and dissipated energy in this direction. On the contrary, the loops coincided in the compression with a less dissipated energy accounting for the lower shear strain of the 10 %C-CHC in this direction. From the comparison of the hysteretic loops in Figs. 14a and 14c, it can be claimed that more energy dissipated in extension direction of the 10 %C-CHC implying that more resilient shear strain occurred in extension direction of the 0 %C-CHC. This can be explained that clay material exhibits less resilient behavior than granular soil due to its higher compressibility behavior under repeated loads. Moreover, the shear strain dramatically dropped to its stable value (as magnitude) in both directions after approximately 2000 load cycles (Fig. 12f). This accounts for the nearly linear hysteretic loop with a very

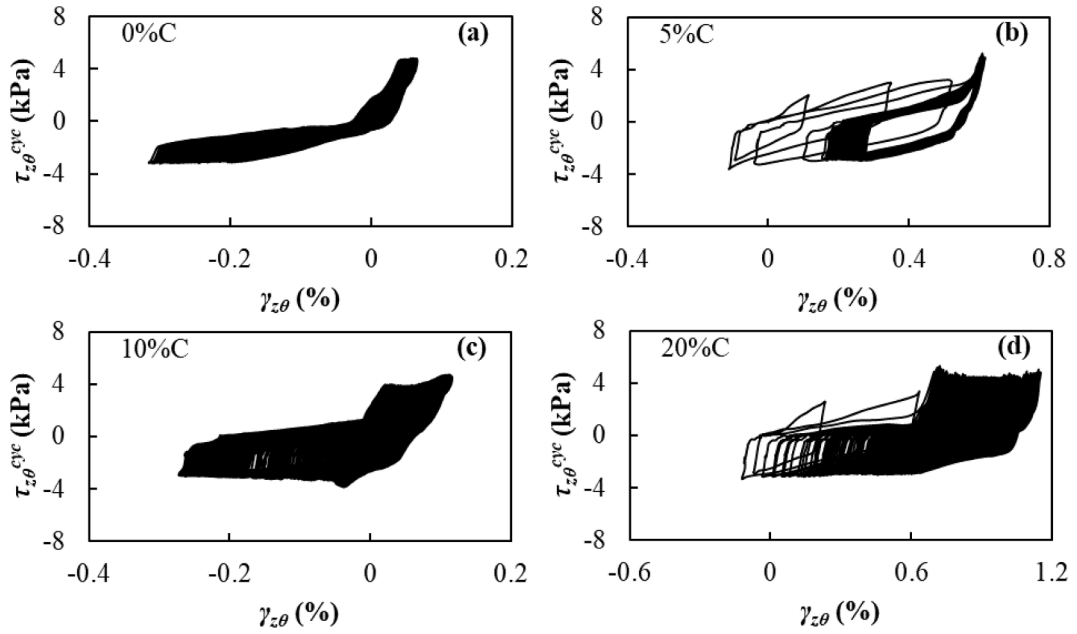

Fig. 13. Torsional shear stress–strain responses of CHC specimens containing a) 0% clay, b) 5% clay, c) 10% clay, and d) 20% clay.

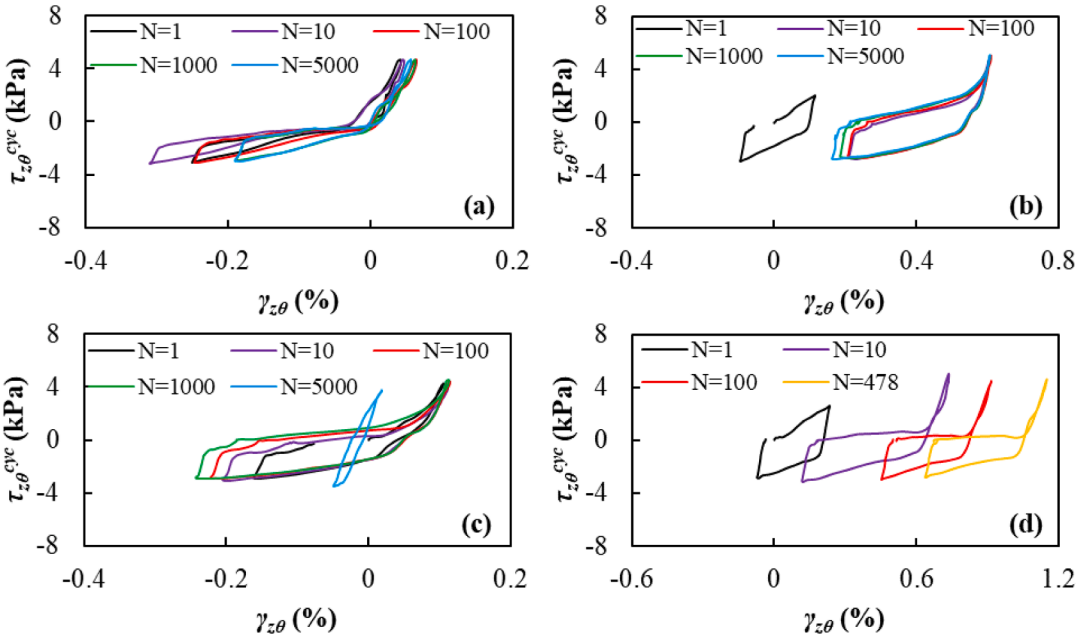

Fig. 14. Torsional shear stress–strain responses at different load cycles: a) CHC specimen with 0% clay; b) CHC specimen with 5% clay; c) CHC specimen with 10% clay; d) CHC specimen with 20% clay.

small dissipated energy at $N = 5000$ (Fig. 14c).

Fig. 14d presents the hysteretic loops of the 20 %C-CHC that are plotted at $N = 1$, 10, 100, and 478. As observed in Fig. 14d, the hysteretic loops progressively shifted to the right as the number of load cycles increased. This means that the shear strain continuously accumulated in this specimen throughout the test. Due to a rapid development of the shear strain in earlier cycles, the target torsional shear stress (4 kPa) was progressively achieved with increasing number of load cycles. Therefore, the lower torsional shear stress was obtained at $N = 1$. As for the dissipated energy, the dissipated energy first increased with increasing number of load cycles and then slightly decreased to a stable level after a small number of load cycles ($N > 10$), indicating that a decrease in increment rate of the shear strain happened after approximately 10 load cycles (Fig. 14h). Therefore, lower energy dissipated at $N = 100$ and $N = 478$ compared to that of at $N = 10$. Moreover, linear parts of the loops in Fig. 14h can be explained that in a loading cycle, an interlocking between sand and clay particles occurs in compression during loading. However, it was adversely affected by the presence of clay during unloading (i.e., loading in reverse direction).

Conclusions

This study experimentally examined the strain behaviors and stress–strain characteristics of medium-dense sand-clay mixtures with 0%, 5%, 10%, and 20% clay by weight under CT and heart-shaped stress paths through a series of cyclic triaxial (CT) and hollow cylinder (CHC)

tests. Based on the test results, the following conclusions can be drawn:

1. The CHC specimens produced larger axial strains than the CT specimens confirming the influence of the PSR induced by a heart shaped stress path. However, despite the larger axial strain behavior in the CHC specimens, the effect of PSR was determined to be small at low clay contents (≤10%) and low *CVSR* (0.15).
2. All specimens except for the 20 %C-CHC carried the applied loads over the whole load cycles ($N = 5000$) without failure ($\varepsilon_z < 0.12\%$). These results showed that the effect of a PSR induced by a heart-shaped stress path may become more apparent in a medium-dense sand-clay mixture as clay content increases (≥20%).
3. The soil behavior changed from an elasto-plastic behavior with perfect plasticity to slightly strain hardening behavior under CT and heart-shaped stress paths due to clay addition. On the other hand, the 20 %C-CHC exhibited strain softening behavior. Furthermore, this mixture produced sparser axial stress–strain hysteretic loops and the axial strain continued to develop until it failed.
4. All specimens except for the 20 %C-CHC exhibited plastic creep behavior under repeated loads while the 20 %C-CHC exhibited ratchetting behavior because of a rapid increase in axial strain.
5. All CHC specimens without failure ($\varepsilon_z < 5\%$) produced shear strain<0.8% over the whole load cycles ($N = 5000$) and reached to a stable position after a finite number of load cycles ($N < 2000$). This can be explained that a better interlocking of soil particles may occur at low stress ratios ($CVSR = 0.15$ and $\eta = 1/3$) and low clay contents (≤10%). However, the 20 %C-CHC specimen yielded increasing shear strain ($\gamma_{z\theta} > 0.8\%$) with *N* indicating that clay inclusion at high content (≥20%) may adversely affect the contact area between sand particles and their interlocking under loads. As a result, a shear strain development in a medium-dense sand clay mixture due to a PSR should be analyzed particularly at high clay contents (≥20%).
6. All CHC specimens generated the shear stress–strain hysteretic loops in asymmetric shapes under loading and unloading directions. The distance between the successive shear stress–strain hysteretic loops decreased in the specimens without failure with increasing number of load cycles. Then, the loops nearly coincided with the previous ones implying that a stable stress–strain behavior was achieved in these specimens after a finite number of load cycles. As for the 20 % C-CHC, the loops progressively shifted to the right for this specimen due to increasing shear strain.
7. It is concluded from the results that a PSR by a heart-shaped stress path should be taken into account to better analyze the strain responses and stress–strain behaviors of the medium-dense sand-clay mixtures under traffic loads.
8. This study mainly focused on the effect of a PSR induced by a traffic loading on the deformation responses of medium-dense sand-clay mixtures containing clay at low rates (≤20% by weight). Based on the findings of this study, it is recommended that different magnitudes of stress ratios (*CVSR* and η), relative densities, and clay contents (>20%) be investigated in future studies to have a better understanding of the deformation behavior of sand-clay mixtures under a PSR induced by traffic loading. Moreover, the critical clay content of medium-dense sand-clay mixtures under a principal stress rotation needs to be studied for different clay contents (between 10% and 20%) and stress ratios in the future.

CRediT authorship contribution statement

Halil Ibrahim Fedakar: Conceptualization, Investigation, Visualization, Writing - original draft. **Bora Cetin:** Supervision, Resources, Writing - review & editing. **Cassandra J. Rutherford:** Supervision, Resources, Writing - review & editing.

Declaration of Competing Interest

The authors declare that they have no known competing financial interests or personal relationships that could have appeared to influence the work reported in this paper.

Acknowledgements

The first author of this study would like to thank the Scientific and Technological Research Council of Turkey (TUBITAK) for the financial support during his postdoctoral research at the Department of Civil, Construction and Environmental Engineering, Iowa State University.

References

Alnedawi A, Nepal KP, Al-Ameri R. Mechanistic behavior of open and dense graded unbound granular materials under traffic loads. Int J Geomate 2018;14(45):124–9. https://doi.org/10.21660/2018.45.7336.

Alnedawi A, Nepal KP, Al-Ameri R. Effect of loading frequency on permanent deformation of unbound granular materials. Int J Pavement Eng 2019. https://doi.org/10.1080/10298436.2019.1656807.

Belkhatir M, Missoum H, Arab A, Della N, Schanz T. Undrained shear strength of sand-silt mixture: Effect of intergranular void ratio and other parameters. KSCE J Civ Eng 2011;15(8):1335–42. https://doi.org/10.1007/s12205-011-1051-x.

Cai YQ, Guo L, Jardine RJ, Yang ZX, Wang J. Stress-strain response of soft clay to traffic loading. Geotech 2017;67(5):446–51. https://doi.org/10.1680/jgeot.15.P.224.

Cai YQ, Sun Q, Guo L, Juang CH, Wang J. Permanent deformation characteristics of saturated sand under cyclic loading. Can Geotech J 2015;52(6):795–807. https://doi.org/10.1139/cgj-2014-0341.

Cai Y, Wu T, Guo L, Wang J. Stiffness degradation and plastic strain accumulation of clay under cyclic load with principal stress rotation and deviatoric stress variation. J Geotech Geoenviron Eng 2018;144(5). https://doi.org/10.1061/(ASCE)GT.1943-5606.0001854.

Cetin A, Kaya Z, Cetin B, Aydilek AH. Influence of laboratory compaction method on mechanical and hydraulic characteristics of unbound granular base materials. Road Mater Pavement Des 2014;15(1):220–35. https://doi.org/10.1080/14680629.2013.869505.

Chai JC, Miura N. Traffic-load-induced permanent deformation of road on soft subsoil. J Geotech Geoenviron Eng 2002;128(11):907–16. https://doi.org/10.1061/(ASCE)1090-0241(2002)128:11(907).

Cheung LW. Laboratory assessment of pavement foundation materials. Ph.D. Thesis, University of Nottingham; 1994.

Cui YJ. Mechanical behaviour of coarse grains/fines mixture under monotonic and cyclic loadings. Transp Geotech 2018;17(A):91–7. https://doi.org/10.1016/j.trgeo.2018.09.016.

Fedakar HI, Cai W, Rutherford CJ, Cetin B. Evaluation of deformation behavior of sand-clay mixture under traffic loads. ASCE Geo-Congress 2020: Vision. Insight, Outlook: MN, USA 2020;2020:201–9.

Frost MW, Fleming PR, Rogers CDF. Cyclic triaxial tests on clay subgrades for analytical pavement design. J Transp Eng 2004;130(3). https://doi.org/10.1061/(ASCE)0733-947X(2004)130:3(378).

Georgiannou VN, Konstadinou M. Effects of density on cyclic behaviour of anisotropically consolidated Ottawa sand under undrained torsional loading. Geotech 2014;64(4):287–302. https://doi.org/10.1680/geot.13.P.090.

Gräbe PJ, Clayton CR. Effects of principal stress rotation on permanent deformation in rail track foundations. J Geotech Geoenviron Eng 2009;135(4):555–65. https://doi.org/10.1061/(ASCE)1090-0241(2009)135:4(555).

Guimaraes ACR, Da Motta LMG, Castro CD. Permanent deformation parameters of fine-grained tropical soils. Road Mater Pavement Des 2019;20(7):1664–81. https://doi.org/10.1080/14680629.2018.1473283.

Guo L, Cai Y, Jardine RJ, Yang Z, Wang J. Undrained behaviour of intact soft clay under cyclic stress paths that match vehicle loading conditions. Can Geotech J 2018;55:90–106. https://doi.org/10.1139/cgj-2016-0636.

Guo L, Chen J, Wang J, Cai Y, Deng P. Influences of stress magnitude and loading frequency on cyclic behavior of K_0-consolidated marine clay involving principal stress rotation. Soil Dyn Earthq Eng 2016;84:94–107. https://doi.org/10.1016/j.soildyn.2016.01.024.

Haider I, Kaya Z, Cetin A, Hatipoglu M, Cetin B, Aydilek AH. Drainage and mechanical behavior of highway base materials. J Irrig Drain Eng 2014;140(6). https://doi.org/10.1061/(ASCE)IR.1943-4774.0000708.

Hight DW, Gens A, Symes MJ. The development of a new hollow cylinder apparatus for investigating the effects of principal stress rotation in soils. Geotech 1983;33(4):355–83. https://doi.org/10.1680/geot.1983.33.4.355.

Hyodo M, Murata H, Yasufuku N, Fujii T. Undrained cyclic shear strength and residual shear strain of saturated sand by cyclic triaxial tests. Soils Found 1991;31(3):60–76. https://doi.org/10.3208/sandf1972.31.3_60.

Hyodo M, Yamamoto Y, Sugiyama M. Undrained cyclic shear behaviour of normally consolidated clay subjected to initial static shear stress. Soils Found 1994;34(4):1–11. https://doi.org/10.3208/sandf1972.34.4_1.

Kim D, Kim JR. Resilient behavior of compacted subgrade soils under the repeated triaxial test. Constr Build Mater 2007;21(7):1470–9. https://doi.org/10.1016/j.conbuildmat.2006.07.006.

Korkiala TL, Dawson A. Relating full-scale pavement rutting to laboratory permanent deformation testing. Int J Pavement Eng 2007;8(1):19–28. https://doi.org/10.1080/10298430600783509.

Li L, Dan H, Wang L. Undrained behavior of natural marine clay under cyclic loading. Ocean Eng 2011;38(16):1792–805. https://doi.org/10.1016/j.oceaneng.2011.09.004.

Li L, Liu J, Zhang X, Li P, Saboundjian S. Characterizing permanent deformation of Alaskan granular base-course materials. J Mater Civ Eng 2019;31(11). https://doi.org/10.1061/(ASCE)MT.1943-5533.0002911.

Mamou A, Priest JA, Clayton CRI, Powrie W. Behaviour of saturated railway track foundation materials during undrained cycling loading. Can Geotech J 2018;55:689–97. https://doi.org/10.1139/cgj-2017-0196.

Noolu V, Mudavath H, Pillai RJ, Yantrapalli SK. Permanent deformation behaviour of black cotton soil treated with calcium carbide residue. Constr Build Mater 2019;223:441–9. https://doi.org/10.1016/j.conbuildmat.2019.07.010.

Puppala AJ, Mohammad LN, Allen A. Permanent deformation characterization of subgrade soils from RLT test. J Mater Civ Eng 1999;11(4):274–82. https://doi.org/10.1061/(ASCE)0899-1561(1999)11:4(274).

Puppala AJ, Saride S, Chomtid S. Experimental and modeling studies of permanent strains of subgrade soils. J Geotech Geoenviron Eng 2009;135(10):1379–89. https://doi.org/10.1061/(ASCE)GT.1943-5606.0000163.

Qian JG, Du ZB, Yin ZY. Cyclic degradation and non-coaxiality of soft clay subjected to pure rotation of principal stress directions. ACTA Geotech 2018;13:943–59. https://doi.org/10.1007/s11440-017-0567-8.

Qian JG, Wang YG, Yin ZY, Huang MS. Experimental identification of plastic shakedown behavior of saturated clay subjected to traffic loading with principal stress rotation. Eng Geol 2016;214:29–42. https://doi.org/10.1016/j.enggeo.2016.09.012.

Saberian M, Li J. Long-term permanent deformation behaviour of recycled concrete aggregate with addition of crumb rubber in base and sub-base applications. Soil Dyn Earthq Eng 2019;121:436–41. https://doi.org/10.1016/j.soildyn.2019.03.029.

Saberian M, Li J, Setunge S. Evaluation of permanent deformation of a new pavement base and subbase containing unbound granular materials, crumb rubber and crushed glass. J Clean Prod 2019;230:38–45. https://doi.org/10.1016/j.jclepro.2019.05.100.

Salgado R, Bandini P, Karim A. Shear strength and stiffness of silty sand. J Geotech Geoenviron Eng 2000;126(5):451–62. https://doi.org/10.1061/(ASCE)1090-0241(2000)126:5(451).

Shen Y, Wang X, Liu HL, Du WH, Wang BG, Xu HD. Influence of principal stress rotation of unequal tensile and compressive stress amplitudes on characteristics of soft clay. J Mt Sci 2017;14(2):369–81. https://doi.org/10.1007/s11629-016-4000-9.

Simpson DC, Evans TM. Behavioral thresholds in mixtures of sand and kaolinite clay. J Geotech Geoenviron Eng 2016;142(2). https://doi.org/10.1061/(ASCE)GT.1943-5606.0001391.

Tao M, Mohammad LN, Nazzal MD, Zhang Z, Wu Z. Application of shakedown theory in characterizing traditional and recycled pavement base materials. J Transp Eng 2010;136:214–22. https://doi.org/10.1061/(ASCE)0733-947X(2010)136:3(214).

Vaid YP, Chern JC. Effect of static shear on resistance to liquefaction. Soils Found 1983;23(1):47–60. https://doi.org/10.3208/sandf1972.23.47.

Vaid YP, Sayao A, Hou E, Negussey D. Generalized stress-path-dependent soil behaviour with a new hollow cylinder torsional apparatus. Can Geotech J 1990;27(5):601–16. https://doi.org/10.1139/t90-075.

Wang Y, Gao Y, Guo L, Yang Z. Influence of intermediate principal stress and principal stress direction on drained behavior of natural soft clay. Int J Geomech 2018;18(1). https://doi.org/10.1061/(ASCE)GM.1943-5622.0001042.

Xiong H, Guo L, Cai YQ, Yang ZX. Experimental study of drained anisotropy of granular soils involving rotation of principal stress direction. Eur J Environ Civ Eng 2015;20(4):431–54. https://doi.org/10.1080/19648189.2015.1039662.

Yang Q, Tang Y, Yuan B, Zhou J. Cyclic stress-strain behaviour of soft clay under traffic loading through hollow cylinder apparatus: Effect of loading frequency. Road Mater Pavement Des 2019;20(5):1026–58. https://doi.org/10.1080/14680629.2018.1428219.

Yin ZY, Chang CS. Modeling cyclic behavior of clay by micromechanical approach. J Eng Mech Div ASCE 2013;139(9):1305–9. https://doi.org/10.1061/(ASCE)EM.1943-7889.0000516.

Yin ZY, Wang JH. A one-dimensional strain-rate based model for soft structured clays. Sci China Tech Sci 2012;55(1):90–100. https://doi.org/10.1007/s11431-011-4513-y.

Yin ZY, Yin JH, Huang HW. Rate-dependent and long-term yield stress and strength of soft Wenzhou marine clay: Experiments and modeling. Mar Georesour Geotech 2015;33(1):79–91. https://doi.org/10.1080/1064119X.2013.797060.

Zhu QY, Yin ZY, Hicher PY, Shen SL. Nonlinearity of one-dimensional creep characteristics of soft clays. ACTA Geotech 2016;11:887–900. https://doi.org/10.1007/s11440-015-0411-y.